Noncontact longitudinal shear wave imaging for the evaluation of heterogeneous porcine brain biomechanical properties using optical coherence elastography

YIRUI ZHU,[1,2] JIULIN SHI,[2] TOMAS E. GOMEZ ALVAREZ-ARENAS,[3] CHENXI LI,[2] HAOHAO WANG,[2] DONG ZHANG,[1] XINGDAO HE,[2,4] AND XIAO WU[1,5]

[1]*School of Physics, Nanjing University, Nanjing, 210093, China*
[2]*School of Testing and Opto-electric Engineering, Nanchang Hangkong University, Nanchang, 330063, China*
[3]*Ultrasonic and Sensors Technologies Department, Information and Physical Technologies Institute, Spanish National Research Council, Serrano 144, 28006, Madrid, Spain*
[4]*hxd@nchu.edu.cn*
[5]*xswu@nju.edu.cn*

Abstract: High-resolution quantification of heterogeneous brain biomechanical properties has long been an important topic. Longitudinal shear waves (LSWs) can be used to assess the longitudinal Young's modulus, but contact excitation methods have been used in most previous studies. We propose an air-coupled ultrasound transducer-based optical coherence elastography (AcUT-OCE) technique for noncontact excitation and detection of LSWs in samples and assessment of the nonuniformity of the brain's biomechanical properties. The air-coupled ultrasonic transducer (AcUT) for noncontact excitation of LSWs in the sample has a center frequency of 250 kHz. Phase-resolved Doppler optical coherence tomography (OCT) was used to image and reconstruct the propagation behavior of LSWs and surface ultrasound waves at high resolution. An agar phantom model was used to verify the feasibility of the experimental protocol, and experiments with *ex vivo* porcine brain samples were used to assess the nonuniformity of the brain biomechanical properties. LSWs with velocities of 0.83 ± 0.11 m/s were successfully excited in the agar phantom model. The perivascular elastography results in the prefrontal cortex (PFC) of the *ex vivo* porcine brains showed that the Young's modulus was significantly higher in the longitudinal and transverse directions on the left side of the cerebral vessels than on the right side and that the Young's modulus of the PFC decreased with increasing depth. The AcUT-OCE technique, as a new scheme for LSW applications in *in vivo* elastography, can be used for noncontact excitation of LSWs in brain tissue and high-resolution detection of heterogeneous brain biomechanical properties.

1. Introduction

In recent years, the development of noninvasive biomechanical property assessment methods based on elastography, such as magnetic resonance elastography (MRE) and ultrasound elastography (USE), has received much attention in the field of brain tissue imaging [1]. Among these techniques, dynamic elastography, which involves measuring the velocity of shear waves generated within brain tissue, has been used to assess various pathological changes in brain tissue elasticity and generate qualitative and quantitative information that can be used to diagnose clinical brain diseases. Several MRE-based studies have shown that the stiffness of brain tissue decreases with age [2–4], and there is also evidence that the elastic properties of different brain regions are closely linked to human behavior [5,6]. In addition, MRE has been widely used to

diagnose brain tumors, such as meningiomas and small or heterogeneous tumors [7,8]. However, the spatial resolution of MRE limits the accuracy of its high-resolution imaging results in small regions of interest. With the development of ultrasound transducer technology [9,10], USE has been increasingly used by clinicians and researchers to assess changes in biological tissue stiffness during disease onset and progression and has been applied in many fields, such as the diagnosis of breast cancer, thyroid, lymph node, prostate, testis, and ocular tissue disease [11–16]. Several studies have applied USE to evaluate healthy neonatal brains and found that the gray matter in the cerebral cortex exhibits higher elasticity than the white matter and caudate nucleus [17]. Some USE studies have also shown that the brain tissue of full-term neonates is significantly more elastic than that of preterm infants [1]. Studies targeting animal models of traumatic brain injury have suggested that USE may be useful for detecting adverse changes in cerebrospinal fluid after mild traumatic brain injury and that this technique may play an important role in clinical diagnosis [18]. In addition, USE can be used to quantitatively assess brain tumor stiffness, which can assist surgeons in brain tumor diagnosis and guide resection [19]. Moreover, previous studies on animal models of ischemic stroke showed that brain tissue stiffness was significantly lower after ischemic stroke compared to the brain tissue stiffness of normal mice, suggesting that USE is a potential method for detecting and assessing changes in brain tissue elasticity after ischemic stroke [20]. However, the resolution of USE is typically approximately 100 μm, which is not sufficient for high-resolution imaging of the cerebral cortex. In addition, the results of USE are affected by the frequency of the transducer, radiofrequency sampling rate, and other factors [21].

Wave-based optical coherence elastography (OCE) has been significant in the detection of the biomechanical properties of *ex vivo* and *in vivo* tissues. As a functional extension of optical coherence tomography (OCT) technology, OCE has several advantages, including being nondestructive, noncontact, having high resolution and obtaining quantitative quantifications [22]. The shear wave OCE technique was initially used to assess the elastic moduli of agar phantoms, which contain biological tissue, based on the direct relationship between the shear wave velocity and shear modulus [23–26]. Surface acoustic waves (SAWs) are also widely used to assess the elastic properties of biological tissues, considering that the OCE imaging depth is in the millimeter range and is generally restricted to the surface boundary region of the medium [27]. In contrast to pure transverse waves, SAWs have both transverse and longitudinal motion components, and their propagation depends on the surface boundary conditions. In addition, for biological tissues with complex boundary conditions, such as the cornea, Lamb waves are widely used in OCE techniques to assess the elastic modulus of corneal tissue [26]. It is worth noting that the velocity of Lamb waves depends not only on the elastic modulus of the cornea itself but also on the corneal thickness, excitation frequency and acoustic properties of the coupling medium at the corneal boundary, which makes the elasticity assessment results more complex [28]. Longitudinal shear waves (LSWs) are a special case of shear waves. When the surface of an elastic medium is excited by a force perpendicular to the surface, an LSW is generated with the same vibration and propagation direction, and the propagation velocity is comparable to the shear wave propagation velocity, so the wave can be detected by an OCE system [28]. Recently, OCE systems have used LSWs to characterize the elastic properties of phantom models and biological tissues. Zhu et al. developed an OCE system with orthogonal and coaxial excitation using a piezoelectric transducer (PZT) and discussed the behavior of LSWs in agar phantoms of different stiffnesses [29,30]. Zvietcovich F et al. discussed the behavior of LSWs excited by excitation sources of different sizes in an agar model and used the LSW model to assess the elastic modulus of isolated murine brain tissue [31]. Liu C H et al. used the LSW model based on a nanobomb OCE system to analyze the biomechanical properties of soft media [32,33]. However, the excitation methods for LSW generation reported in previous works are contact PZT or laser pulse-based methods, and nondestructive, noncontact excitation of LSWs in biological tissues remains a challenge [31,32]. Acoustic radiation force excitation, employing

ultrasound pulses to generate mechanical waves in tissue, is widely used in OCE technology [22,25]. In previous literature reports, focused ultrasound transducers with different focal lengths and center frequencies have been designed for mechanical excitation of various biological tissues [22]. Additionally, in our previous work, we developed a single-element transmitting ultrasound transducer for corneal tissue elastography, simplifying the OCE system [34]. Notably, air-coupled ultrasound has recently been proposed for use in the field of OCE as a non-contact excitation method. Combining the Lamb wave model and different resolving methods, the OCE technique using air-coupled ultrasound has been used to evaluate the biomechanical properties of the cornea *in vivo* [35–38]. In addition, Wang et al. discussed the behavior of surface acoustic wave in soft tissues using air-coupled ultrasound combined with OCE technique [39].

In this work, we propose the use of an air-coupled ultrasound transducer (AcUT) for noncontact excitation of LSWs and examine the behavior of LSWs in brain tissue using an OCE system to assess the nonuniform elastic modulus of brain tissue. To the best of our knowledge, this is the first time that acoustic radiation force excitation has been used to achieve noncontact excitation of LSWs, and our study presents a new approach for using LSWs for *in vivo* elasticity assessment of biological tissues.

2. Materials and methods

2.1. Phantom preparation

Here, we constructed an agar phantom simulating soft tissue samples at a concentration of 0.3% w/v to verify the feasibility of the LSW-based noncontact excitation method. Agar was dissolved in distilled water at 25 °C, and the solution was then heated to 95 °C. After stopping the heating, the agar solution was cooled to 60 °C, and 0.06% v/v of the internal lipid solution was mixed with the agar solution to increase light scattering. After stirring for 5 min, the final solution was stored in a refrigerator at 4 °C for curing. A density of 1000 kg/m^3 was used to calculate the shear modulus of the phantom.

2.2. Ex vivo porcine brain preparation

Brain tissue was obtained from pigs within two hours of death. An air-coupled ultrasound transducer was used to excite elastic waves in brain tissue without contact, so no coupling agents were used. During the experiment, 2% artificial cerebrospinal fluid was added by syringe drip at room temperature (25 °C) to maintain brain tissue freshness. After the experiments were completed, the *ex vivo* porcine brain tissue was immersed in formalin solution for preservation.

2.3. Air-coupled ultrasound transducer-based OCE (AcUT-OCE) system design

We developed an AcUT-OCE system for noncontact detection of elastic wave propagation processes in brain tissue, and the schematic diagram of the proposed system is shown in Fig. 1(a). The acoustic radiation force excitation part consists of a function generator, a power amplifier, and an air-coupled ultrasonic transducer. The AcUT has a center frequency of 250 kHz, a focal length of 60 mm, an output sound field with an approximate Gaussian distribution, and a focal spot diameter of approximately 4 mm. The AcUT is housed in an aluminum alloy package with grounding, has an outside diameter of approximately 25 mm and is connected to the power amplifier via a BNC cable. The function generator produces a sine wave burst signal with a center frequency of 250 kHz, which is amplified by the power amplifier to drive the AcUT to generate ultrasonic waves. The phase-resolved OCT system uses a swept laser with a central wavelength of 1310 nm, a scanning bandwidth of 100 nm, and an A-line speed of 50 kHz. The OCT system has a lateral resolution of 15 μm, an axial resolution of 5.7 μm, an imaging depth of approximately 3 mm, and a signal-to-noise ratio of 105. The M-B scan mode was used to detect and reconstruct the elastic wave propagation process, as shown in Fig. 1(b). Specifically,

an M-scan was completed by repeating the A-line scan 500 times at each sampling point, and then a two-dimensional (2D) galvanometer moved the detection beam to the next sampling point and repeated the M-scan. A total of 1000 M-scans were performed in the transverse direction to complete the entire M-B scan, which took 5 s in total. The synchronization timing between the acoustic radiation force and the optical detection was controlled via an NI card. For each M-scan, the acoustic radiation force was applied during the 121st and 140th A-line scans, lasting a total of 400 μs.
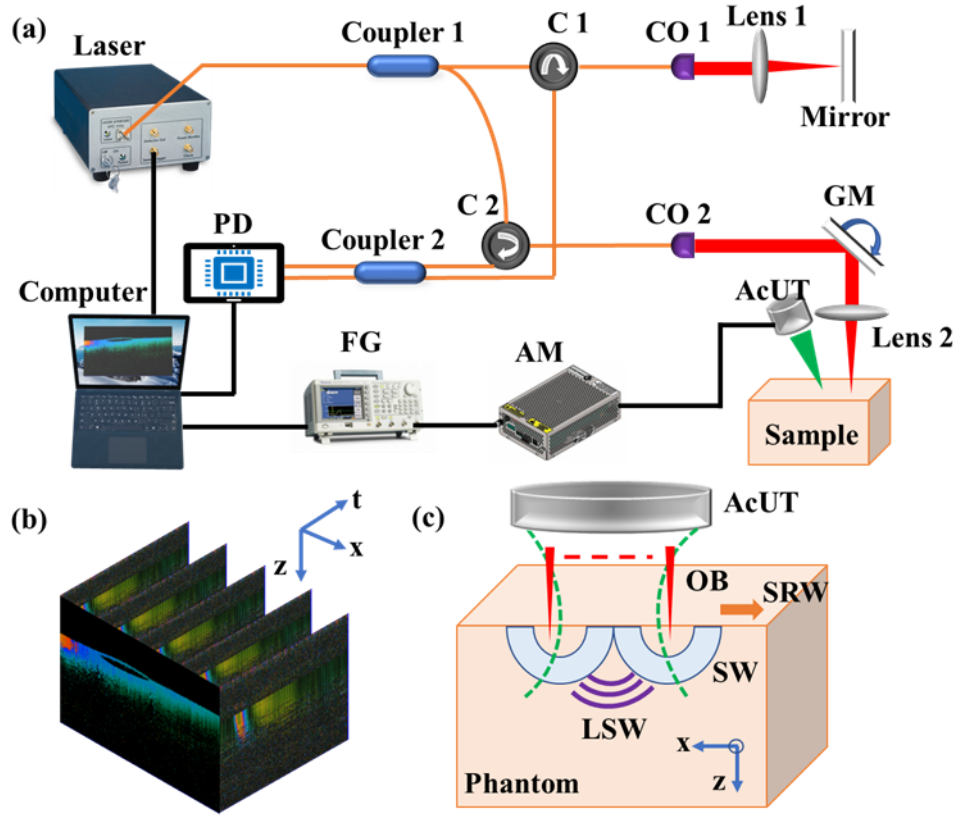
Fig. 1. (a) Schematic diagram of the AcUT-OCE system; C1: Circulator 1, C2: Circulator 2, CO1: Collimator 1, CO2: Collimator 2, GM: Galvanometer, FG: Function generator, AM: Amplifier, PDB: Photoelectric detector. (b) 3D M-B scan mode (x, z, t). (c) Diagram of the LSW generation process via AcUT noncontact excitation; LSW: Longitudinal shear wave, SW: Shear wave, SAW: Surface acoustic wave, OB: Optical beam.

2.4. Longitudinal shear wave model and calculation of the shear modulus

The Green's function solution includes the harmonic forms of the near-field longitudinal and transverse waves [40]:

$$G_{mn}(0,r) = \frac{1}{4\pi\rho\alpha^2}\frac{\gamma_m\gamma_n}{r}e^{iqr} - \frac{1}{4\pi\rho}\frac{3\gamma_m\gamma_n - \delta_{mn}}{r^3}\frac{e^{iqr}}{i\omega}\left(\frac{r}{\alpha} - \frac{1}{i\omega}\right)$$

$$+\frac{1}{4\pi\rho\beta^2}\frac{\delta_{mn}-\gamma_m\gamma_n}{r}e^{ikr} + \frac{1}{4\pi\rho}\frac{3\gamma_m\gamma_n-\delta_{mn}}{r^3}\frac{e^{iqr}}{i\omega}\left(\frac{r}{\beta} - \frac{1}{i\omega}\right),$$

$$G_{mn}(0,r) = G_{mn}^{L} + G_{mn}^{NFP} + G_{mn}^{T} + G_{mn}^{NFS} = G_{mn}^{P} + G_{mn}^{S}$$

(1)

where α and β are the longitudinal and shear wave velocities, respectively, r is the radial distance to the excitation point, and q and k are the dilatational and shear wavenumbers, respectively. ω is the angular frequency, and $\gamma_i = x_i/r$ is the direction cosine measure. In this expression, the divergence-free term G_{mn}^S can be interpreted as shear S waves, and G_{mn}^{NFS} has been shown to have longitudinal polarization and is referred to as a longitudinal shear wave.

In this study, the focal point of the acoustic radiation force is 4 mm in diameter, and when the acoustic radiation force is excited perpendicular to the surface boundary of the medium, surface acoustic waves (SAWs) in the near field and LSWs parallel to the excitation direction are generated, as has been demonstrated in previous works [31]. As shown in Fig. 1(c), after the excitation of the acoustic radiation force, the superposition of multiple near-field shear waves leads to the formation of a longitudinal shear wave with a propagation velocity close to that of the shear wave. Therefore, the Young's modulus can be calculated as:

$$E = 2 \times \rho \times (1 + \nu) \times c_s^2 \tag{2}$$

where E is the Young's modulus, ρ and ν are the density and Poisson ratio of the sample, respectively, and c_s is the velocity of the shear wave.

The SAW propagates along the surface and penetrates to a depth on the order of a wavelength, and its propagation speed is dependent on the boundary conditions. We use an air-coupled ultrasonic transducer to excite the acoustic radiation force, thereby avoiding the use of coupling agents; thus, the medium can be considered a free boundary surface, and the relationship between the velocity of the SAW and the shear wave velocity is:

$$c_{SAW} \approx 0.97 \, c_s \tag{3}$$

where c_{SAW} is the velocity of the SAW. The relationship between the Young's modulus and the SAW velocity is:

$$E = 2 \times \rho \times \frac{(1+\nu)^3}{(0.87+1.12\nu)^2} \times c_{SAW}^2 \tag{4}$$

We can therefore evaluate the Young's modulus characterized by the longitudinal shear waves and surface waves separately to evaluate the differences in the biomechanical properties of brain tissue in different directions.

In the elastic wave detection process, the mechanical perturbation caused by the acoustic radiation force changes the phase of the backscattered light, and the relationship between the particle vibration velocity c_z and the phase difference signal $\Delta\emptyset(z)$ can be calculated using the phase-resolved Doppler algorithm as:

$$c_z = \Delta\emptyset(z)\frac{\lambda_0}{4\pi nT} \tag{5}$$

where λ_0 is the center wavelength, n is the refractive ratio, and T is the A-line sampling time.

3. Results

3.1. LSW propagation results in the phantom

Although we have evaluated the reliability and accuracy of the OCE system in previous work using uniaxial tensile testing, [41], this is the first time it has been used for non-contact LSW imaging of OCE. Therefore, we first completed homogeneous agar phantom experiments to verify the feasibility of the noncontact LSW excitation method via air-coupled ultrasonic transducers. As shown in Fig. 2(a), for the M-mode OCE imaging results, unlike the propagation velocity of longitudinal waves, LSWs propagate at the transverse velocity and require more time to propagate from the agar surface along the depth direction. For the area marked with white

arrows in Fig. 2(a), the vibration displacement curves of the LSWs along the depth direction at different detection moments are shown in Fig. 2(b), and the results show that the wave crest of the vibration displacement propagates along the depth direction. In the calculation of the LSW group velocity, the propagation distance corresponding to the time contour is calculated along the depth direction, as shown in Fig. 2(a), and this value can be expressed as the tangent of angle θ, $\tan(\theta) = \Delta z / \Delta t$, which is approximately 0.83 ± 0.11 m/s. The SAW detection results in the agar phantom are shown in Fig. 3. Figures 3(a)-(b) show the propagation process of the SAW vibration displacement at different moments. When the acoustic radiation force is excited, the SAW propagates from the excitation point to the surrounding area, and the different colors represent various vibration directions. When the 3D data obtained from the M-B scanning mode are resliced along the depth direction, the spatiotemporal displacement map of the SAW at each depth can be obtained, as shown in Fig. 4 for the depth identified by the white line in Fig. 3(a). The propagation velocity of the SAW, which can be obtained by calculating the propagation distance of the SAW in the detection time, is approximately 1.11 ± 0.20 m/s, which is consistent with the results reported in the previous literature [31].
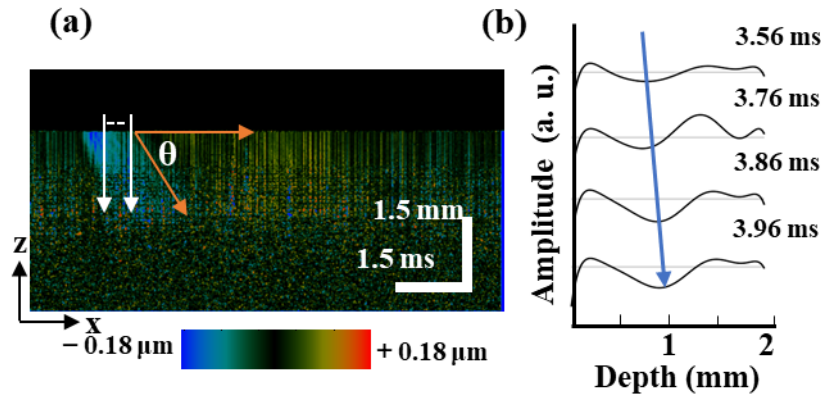

Fig. 2. The LSW results in a phantom. (a) M mode image result, with the white arrows indicating different detection moments. (b) Vibration displacement curve of the LSW in the depth direction at different detection moments.

3.2. LSW propagation results in ex vivo porcine brain tissue

For the brain tissue experiments, fresh porcine brains within two hours of death were selected as samples, as shown in Fig. 5(a). During the experiments, the prefrontal cortex (PFC) region of the porcine brain was selected for imaging, and this region is marked by the white arrow in Fig. 5(a). Cerebrovascular structures were present in the scanned region, as shown in Fig. 5(b), and the results reveal significant differences in the brain tissue structures on the left and right sides of the vessels, which are marked by orange and blue arrows, respectively. We also performed 3D imaging scans of the PFC, and the results are shown in Fig. 5(c). Obvious nonuniform structures can be observed on the left and right sides of the cerebral vessels, which are marked with red arrow.

Differences in biological tissue structures often lead to differences in biomechanical properties; thus, the propagation process of the LSW was evaluated separately for the left and right sides of the cerebral vessels in the PFC region. Figure 6 shows the LSW propagation results in the PFC region. The M-mode imaging results of the LSWs at the location marked by the orange arrow in Fig. 5(b) are shown in Fig. 6(a), and the vibration displacement curves of the LSW at different times along the depth direction in the region marked by the white arrow are shown in Fig. 6(c). The yellow arrow marks the depth of the vibration displacement wave crest. The
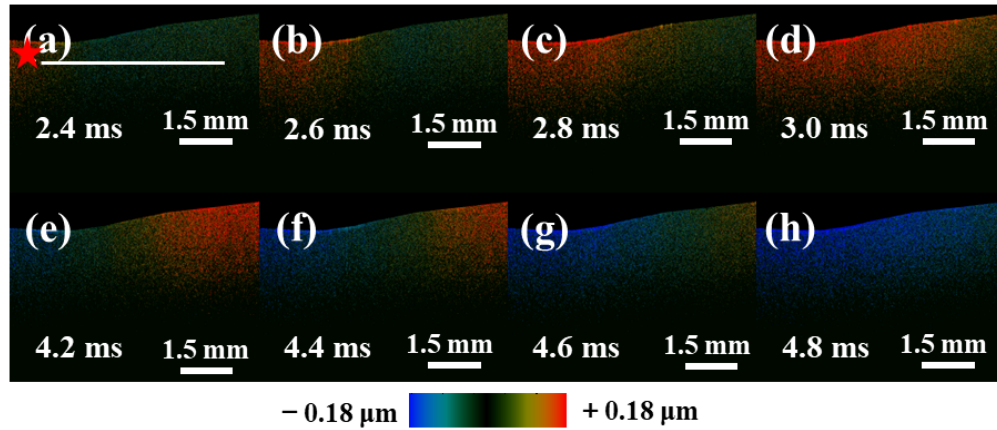
Fig. 3. The propagation process of the SAW vibration displacement at different times. (a) The red star indicates the AcUT excitation point, and the white line indicates the depth at which the SAW velocity is calculated.
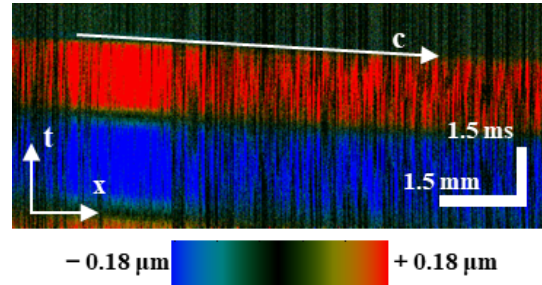

Fig. 4. The spatiotemporal displacement map of the SAW at the depth marked by the white line in Fig. 3(a).
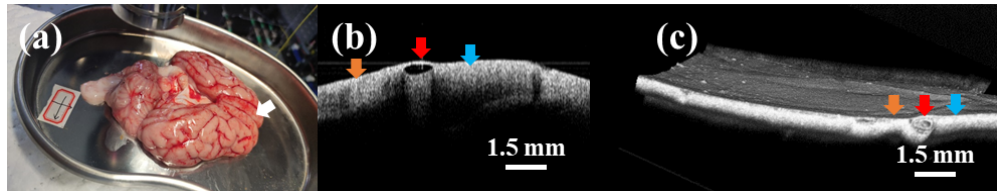

Fig. 5. *Ex vivo* porcine brain structural results. (a) Picture of *ex vivo* porcine brain tissue; the white arrow marks the PFC region. (b) 2D OCT structure result of the PFC, with the orange and blue arrows indicating nonuniform structures, and the red arrow indicating the blood structure. (c) 3D OCT reconstruction result of the PFC.

vibration envelope of the LSW propagates to a deeper position over time, and the speed of the LSW is calculated to be 1.26 ± 0.21 m/s. The M-mode imaging results of the LSW propagation process at the position marked by the blue arrow on the right side of the cerebral vessels in the PFC region in Fig. 5(b) are shown in Fig. 6(b). Similarly, the vibration displacement curves of the LSW at different times along the depth direction are shown in Fig. 6(d). At the same moment of detection, the vibration displacement envelope propagates over a shorter distance on the right side of the cerebral vessel than on the left side of the cerebral vessel (Fig. 6(c)), and the velocity of the LSW is calculated to be 0.95 ± 0.14 m/s.
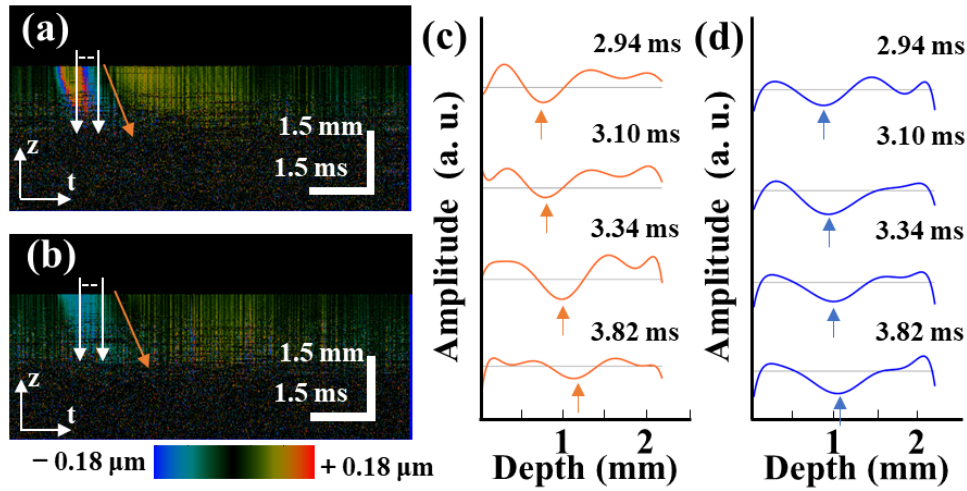
Fig. 6. LSW propagation in the PFC region of the brain. (a) LSW M-mode imaging result on the left side of the cerebral vessels in the PFC. (b) LSW M-mode imaging result on the right side of the cerebral vessels in the PFC. (c) Vibration displacement curve of LSW propagation at different times at the location marked by the white arrows in (a). (d) Vibration displacement curve of LSW propagation at different times at the location marked by the white arrows in (b).
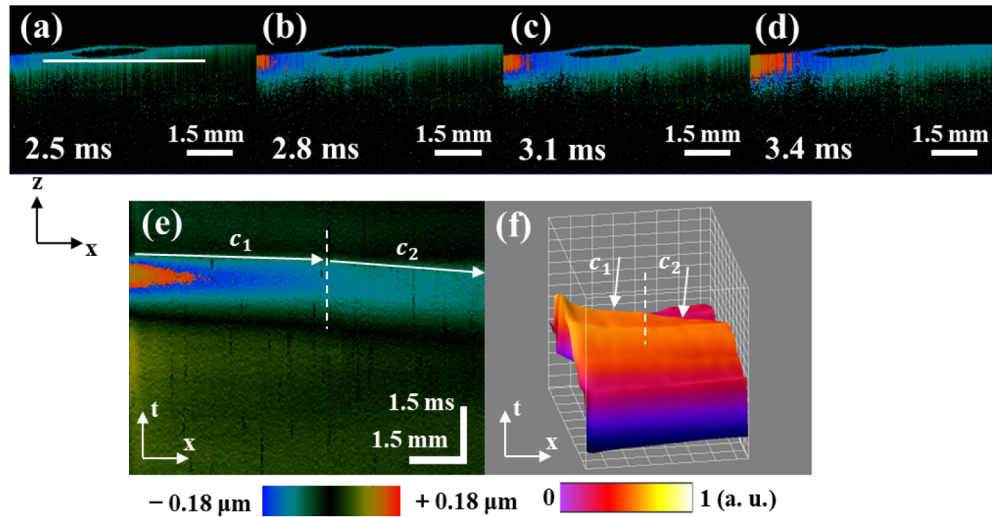

Fig. 7. SAW propagation results. (a)-(d) Motion snapshots of the vibration displacement of the SAW at different detection times. (e) Spatiotemporal displacement map of the SAW. (f) 3D surface reconstruction result of the SAW spatiotemporal displacement map.

The SAW imaging results are shown in Fig. 7. The motion snapshots of the SAW vibration displacement at different detection times are shown in Fig. 7(a)-(d). The SAW propagates from the left excitation position to the right, and its amplitude decays after the wave passes through the cerebral vascular structures. The 3D M-B scan mode data obtained in the brain tissue are resliced along the depth direction at the depth marked by the white line in Fig. 7(a), and the spatiotemporal displacement map of the SAW along the lateral propagation direction is obtained,
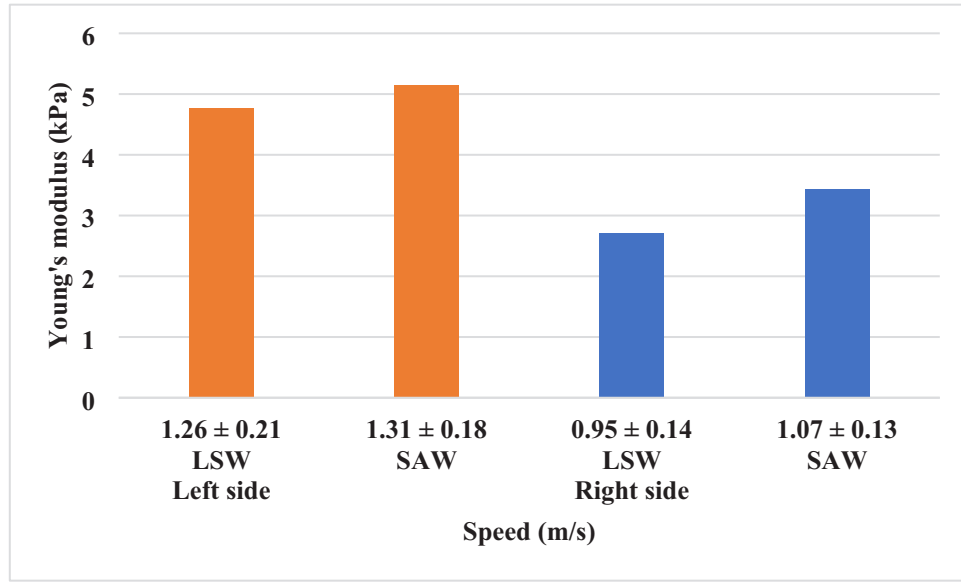
Fig. 8. Young's modulus results of the *ex vivo* porcine brain tissue at different lateral positions.
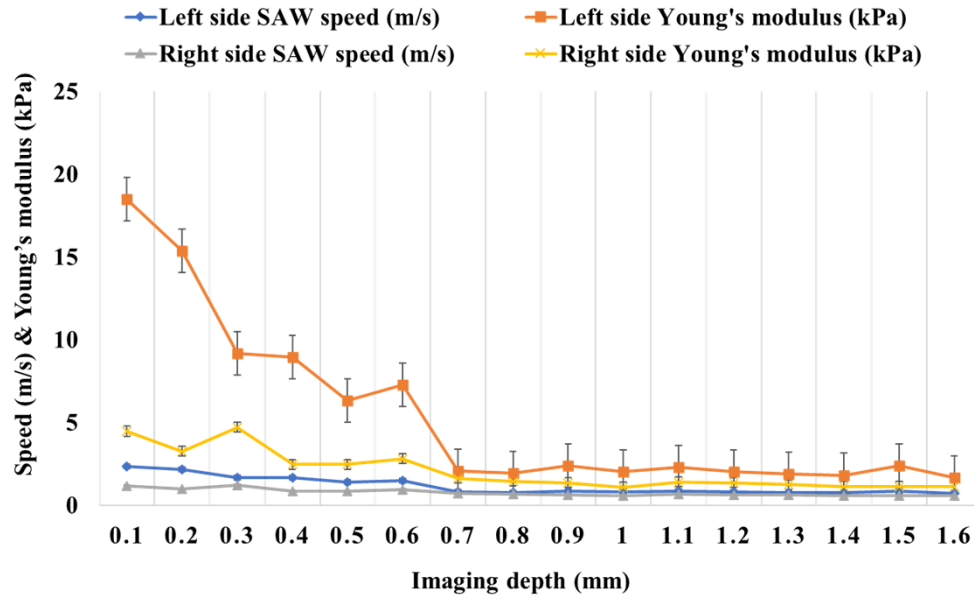
Fig. 9. Calculation of the Young's modulus of the brain tissue at different depths.

as shown in Fig. 7(e). The temporal contour of the SAW has two different slopes along the lateral direction, which are distributed on the left and right sides of the cerebral vessels, as marked by the white dashed line. We then reconstructed the spatiotemporal displacement map of the SAW in three dimensions and obtained its surface morphology, as shown in Fig. 7(e). The temporal contours on the left and right sides of the white dashed line have different slopes, which suggests that the SAW has a different propagation speed in this region. The velocities c_1 and c_2 of the

SAW are calculated to be 1.31 ± 0.18 m/s and 1.07 ± 0.13 m/s on the left and right sides of the vessels, respectively.

3.3.　Shear modulus results of ex vivo porcine brain tissue

Brain tissue is usually considered to be an incompressible biological tissue with a Poisson's ratio of approximately 0.5 and a density of $1000 \, \text{kg/cm}^3$, and the Young's modulus based on the LSW and SAW velocities are calculated according to Eqs. (2) and (4), respectively. Here, t tests were used to assess the difference between the LSW and SAW results in brain tissue, and a P value less than 0.05 was considered statistically significant. As shown in Fig. 8, the LSW and SAW velocities are both greater on the left side of the cerebral vessels than on the right side ($P < 0.05$) at different lateral positions. This result implies that the Young's modulus is greater on the left side of the cerebral vessels than on the right side, indicating the nonuniformity of the biomechanical properties of brain tissue. In addition, the propagation velocities of the LSW and SAW in brain tissue were not significantly different. For different longitudinal depths of the brain tissue, we evaluated the propagation velocity of the SAW with the corresponding Young's modulus at 0.1 mm intervals on the left and right sides of the cerebral vessels, as shown in Fig. 9. In the 0.7 mm depth range, which is marked with green in the figure, the Young's modulus of the brain tissue decreased by more than 50% with increasing depth on both the left and right sides of the cerebral vessels, and the Young's modulus was higher in the left region than in the right region. Moreover, the Young's modulus of the brain tissue did not change significantly after a depth of 0.7 mm.

4.　Discussion

Longitudinal shear waves (LSWs) propagate axially at velocities comparable to shear wave velocities and can therefore be detected by OCE technology and used to assess the anisotropic biomechanical properties of tissues, such as muscles and nerves. However, contact excitation methods have been widely used to excite LSWs in previous studies, such as piezoelectric transducers (PZTs), which can obtain high signal-to-noise ratio vibration displacement data but are limited for performing *in vivo* imaging of biological tissues, such as ocular tissue and brain tissue [30,31]. In this study, we present an optical coherence elastography (OCE) system based on an air-coupled ultrasonic transducer (AcUT) for noncontact excitation of LSWs in samples and evaluate the propagation velocities of LSWs and surface acoustic waves (SAWs). To the best of our knowledge, this is the first time that acoustic radiation force technology was used for the noncontact excitation of LSWs in brain tissue and for the assessment of the nonuniformity of the biomechanical properties of brain tissue in different regions and at different depths.

Similar to conventional acoustic radiation force excitation devices, the ultrasonic pulse generated by the air-coupled ultrasonic transducer can be focused at the sample tissue surface through an air medium. Since the acoustic impedance values of air and the sample tissue are often very different, the acoustic radiation energy can be efficiently converted into vibrational displacement in the tissue and generate wave propagation [39]. Alternatively, air-coupled ultrasound transducers can be used to generate elastic waves with large bandwidths, as in the PZT excitation mode, which are considered to be noncontact and therefore more suitable for *in vivo* excitation in biological tissues [38]. In this study, an air-coupled ultrasonic transducer with a center frequency of 250 kHz, a focal length of approximately 60 mm, and a focal diameter of approximately 4 mm was used. Thus, noncontact excitation of LSWs can be achieved when the air-coupled ultrasonic transducer is used to vertically excite the sample surface. The experimental results of the agar phantom model show that when the air-coupled ultrasonic transducer is used to excite the sample, the peak of the axial vibration displacement propagates to different depths with increasing probe time, which indicates that LSWs are successfully excited, as shown in Fig. 2(b). The speed of the LSW in the phantom is approximately 0.83 ± 0.11 m/s, and the propagation

depth is approximately 2 mm. In addition, because the air-coupled ultrasonic transducer focuses the ultrasonic waves on the sample surface, for a semi-infinite space agar model, SAWs are generated and propagate along the surface boundary. We evaluated the behavior of SAWs in the agar model, and the air-coupled ultrasonic transducer excited SAWs with wavelengths of approximately 6.45 mm, while the SAW velocity was approximately 1.11 ± 0.20 m/s, which was not significantly different from the LSW velocity.

The prefrontal cortex (PFC), the cerebral cortex region that includes the frontal lobes, performs judgment and executive functions through extensive connections with different brain regions. If this brain area is damaged, cognitive control is impacted, and the biomechanical properties of brain tissue are an important factor for the normal physiological function of the PFC. OCE experiments were completed using *ex vivo* porcine brain tissue, and the Young's modulus of the PFC was calculated in the longitudinal and transverse directions using the LSW and SAW velocities, respectively. The nonuniformity of the biomechanical properties of the brain tissue was evaluated near the vessels in the PFC, as shown in Fig. 5. The behavior of the LSWs in the transverse direction was first evaluated on the left and right sides of the cerebral vessels, and the velocities of the LSWs in the imaging depth rage with high signal-to-noise ratio were calculated to be 1.26 ± 0.21 m/s and 0.95 ± 0.14 m/s on the left and right sides, corresponding to Young's moduli of 4.76 kPa and 2.71 kPa in the axial direction, respectively. Then, the vibration displacement propagation process of the SAW was reconstructed along the transverse direction, and the SAW velocities on the left and right sides of the cerebral vessels were calculated to be 1.31 ± 0.18 m/s and 1.07 ± 0.13 m/s, respectively, corresponding to Young's moduli of 5.70 kPa and 3.81 kPa. Therefore, the LSW and SAW velocity results show that the stiffness of the region on the left side of the brain vessels in the imaging area is higher than that of the right region, as shown in Fig. 8. In addition, the SAW propagation velocity was quantified at 0.1 mm intervals along the axial direction at different imaging depths. The results are shown in Fig. 9, and the Young's moduli of the regions on the left and right sides of the cerebral vessels decrease with the increasing depth. However, after a depth of 0.7 mm, there is no longer a significant decrease, as marked by the green. At different imaging depths, the Young's modulus on the left side of the cerebral vessels was significantly higher than that on the right side. For brain tissue in the region to the left of the cerebral vasculature, the Young's modulus was significantly higher in the 0.2 mm depth range, which we believe may be because the brain tissue in this region becomes dry due to the decrease in water content in response to the acoustic radiation force.

The heterogeneous nature of the biomechanical properties of brain tissue has been of interest to many researchers. These properties have been used to detect and localize tumor tissue and assess local lesions and damage to brain tissue. Yann et al. used MRE to assess the differences in the biomechanical properties of three types of implanted malignant glial tumors and normal brain tissue, and the results showed that the elastic modulus and viscosity coefficient of tumor tissue were significantly lower than those of normal brain tissue [42]. Jin et al. evaluated the biomechanical properties of different brain regions using tensile and compressive experiments, and the results showed that the white matter is more rigid than the gray matter [43]. Prange et al. found that the corona radiata is harder than the corpus callosum [44]. Fernando et al. evaluated the biomechanical properties of isolated murine brain tissue using a contact LSW imaging method based on the OCE technique [31]. The results showed that the LSW speed in the cerebral cortes are approximately 3.21 ± 0.51 m/s and gradually decrease to approximately 0.94 ± 0.36 m/s in the midbrain and cerebellum, which demonstrate differentiated elasticity values between the cerebral cortex and cerebellum midbrain regions. Our experimental results show that the OCE technique can be used to non-contact quantify the Young's modulus of brain tissue with micrometer resolution, and the OCE results are sensitive to the transverse and longitudinal Young's modulus of brain tissue, as determined with different mechanical wave models. Our experimental results preliminarily indicate that the elastic membrane of isolated porcine brain

tissue decreases from the cerebral cortex in the depth direction, these results are generally consistent with the results reported in the literature [31]. Thus, the AcUT-OCE technique can be used to accurately evaluate the nonuniformity of the biomechanical properties of brain tissue, and our approach has the advantages of being noncontact and obtaining high-resolution results. The OCE technique can be used to distinguish tumor tissue boundaries with high resolution and elastically characterize different stratified structures in the cerebral cortex.

There are some limitations that need to be discussed. First, despite the advantages of high-resolution imaging, the micron-level penetration depth of the OCE technique limits the ability of our system to image deep regions of brain tissue; thus, the OCE technique is more suitable for elasticity detection in cortical brain regions. With the development of advanced ultrasound transducer technology, acoustic radiation force excitation has been widely used for mechanical excitation of biological tissues [11]; however, the safety of air-coupled ultrasound transducers needs to be evaluated in detail to ensure that this technology is suitable for safe excitation of *in vivo* imaging. In this study, *ex vivo* porcine brain tissue was used directly in imaging experiments, and these *ex vivo* experiments may differ from *in vivo* conditions in terms of brain tissue physiological activity, such as the water content, cerebrospinal fluid environment, and skull boundary conditions. Therefore, to accurately assess the elastic modulus of brain tissue, *in vivo* brain tissue experimental protocols should be designed, such as using the brain tissue optical window technique. In addition, we only completed the LSW imaging experiments with a single homogeneous agar and did not address the discussion of multilayered nonhomogeneous samples. Finally, brain tissue has a water content of more than 80% and is widely understood to be a superviscoelastic material; therefore, the viscoelastic coefficient of brain tissue is an important biomechanical property of brain tissue [45]. Designing experiments with viscoelastic samples and multilayered nonuniform samples can help us to further validate the feasibility and accuracy of the OCE technique and noncontact LSW imaging for viscoelastic evaluation of brain tissues. However, this property is beyond the scope of this work, and we will discuss the viscoelastic properties of brain tissue in detail in future work.

5. Conclusion

In conclusion, we propose an air-coupled ultrasound transducer for noncontact excitation of longitudinal shear waves in brain tissue and employ a phase-resolved Doppler OCT system to detect and reconstruct the propagation behavior of longitudinal shear waves and surface ultrasound waves in brain tissue with high resolution, which is, to the best of our knowledge, the first report on such a technique. We first verified the feasibility of the study protocol using an agar phantom model, and the experimental results showed that LSWs were successfully excited in the agar phantom, and the calculated LSW and SAW results were consistent with those reported in the literature. Furthermore, we evaluated the nonuniformity of the biomechanical properties of the brain areas near the cerebral vessels in the PFC region using isolated porcine brain samples, and the experimental results showed that the Young's modulus in both the transverse and longitudinal directions was significantly higher on the left side of the cerebral vessels than on the right side. Moreover, the Young's modulus of the brain tissue decreased with increasing depth, which indicated that our proposed noncontact OCE system could be used for high-resolution imaging and the detection of the nonuniform biomechanical properties of brain tissue. Thus, our proposed noncontact OCE system can be used for high-resolution imaging of the heterogeneous biomechanical properties of brain tissue and may be a new approach for LSW applications in *in vivo* experiments to assess the longitudinal Young's modulus.

References

1. J. Liao, H. Yang, J. Yu, X. Liang, and Z. Chen, "Progress in the application of ultrasound elastography for brain diseases," Journal of Ultrasound in Medicine **39**(11), 2093–2104 (2020).
2. A. Arani, M. C. Murphy, K. J. Glaser, A. Manduca, D. S. Lake, S. A. Kruse, C. R. Jack Jr, R. L. Ehman, and J. Huston 3rd, "Measuring the effects of aging and sex on regional brain stiffness with MR elastography in healthy older adults," Neuroimage **111**, 59–64 (2015).
3. I. Sack, K.-J. Streitberger, D. Krefting, F. Paul, and J. Braun, "The influence of physiological aging and atrophy on brain viscoelastic properties in humans," PloS one **6**(9), e23451 (2011).
4. I. Sack, B. Beierbach, J. Wuerfel, D. Klatt, U. Hamhaber, S. Papazoglou, P. Martus, and J. Braun, "The impact of aging and gender on brain viscoelasticity," Neuroimage **46**(3), 652–657 (2009).
5. H. Schwarb, C. L. Johnson, M. D. McGarry, and N. J. Cohen, "Medial temporal lobe viscoelasticity and relational memory performance," Neuroimage **132**, 534–541 (2016).
6. H. Schwarb, C. L. Johnson, A. M. Daugherty, C. H. Hillman, A. F. Kramer, N. J. Cohen, and A. K. Barbey, "Aerobic fitness, hippocampal viscoelasticity, and relational memory performance," Neuroimage **153**, 179–188 (2017).
7. J. D. Hughes, N. Fattahi, J. Van Gompel, A. Arani, F. Meyer, G. Lanzino, M. J. Link, R. Ehman, and J. Huston, "Higher-resolution magnetic resonance elastography in meningiomas to determine intratumoral consistency," Neurosurgery **77**(4), 653–659 (2015).
8. M. C. Murphy, J. Huston, K. J. Glaser, A. Manduca, F. B. Meyer, G. Lanzino, J. M. Morris, J. P. Felmlee, and R. L. Ehman, "Preoperative assessment of meningioma stiffness using magnetic resonance elastography," J. Neurosurg. **118**(3), 643–648 (2013).
9. X. Wan, P. Chen, Z. Xu, X. Mo, H. Jin, W. Yang, S. Wang, J. Duan, B. Hu, and Z. Luo, "Hybrid-piezoelectret based highly efficient ultrasonic energy harvester for implantable electronics," Adv. Funct. Mater. **32**(24), 2200589 (2022).
10. Z. Xu, X. Wan, X. Mo, S. Lin, S. Chen, J. Chen, Y. Pan, H. Zhang, H. Jin, and J. Duan, "Electrostatic assembly of laminated transparent piezoelectrets for epidermal and implantable electronics," Nano Energy **89**, 106450 (2021).
11. J. Zhang, J. Murgoitio-Esandi, X. Qian, R. Li, C. Gong, A. Nankali, L. Hao, B. Y. Xu, K. K. Shung, and A. Oberai, "High-frequency ultrasound elastography to assess the nonlinear elastic properties of the cornea and ciliary body," IEEE Transactions on Ultrasonics, Ferroelectrics, and Frequency Control **69**(9), 2621–2629 (2022).
12. R. Li, X. Qian, C. Gong, J. Zhang, Y. Liu, B. Xu, M. S. Humayun, and Q. Zhou, "Simultaneous assessment of the whole eye biomechanics using ultrasonic elastography," IEEE Transactions on Biomedical Engineering (2022).
13. X. Qian, R. Li, G. Lu, L. Jiang, H. Kang, K. K. Shung, M. S. Humayun, and Q. Zhou, "Ultrasonic elastography to assess biomechanical properties of the optic nerve head and peripapillary sclera of the eye," Ultrasonics **110**, 106263 (2021).
14. B. Zeng, F. Chen, S. Qiu, Y. Luo, Z. Zhu, R. Chen, and L. Mao, "Application of quasistatic ultrasound elastography for examination of scrotal lesions," Journal of Ultrasound in Medicine **35**(2), 253–261 (2016).
15. Z. Hu, Y. Li, C. Li, C. Huang, Z. Ou, J. Guo, H. Luo, and X. Tang, "Using ultrasonic transient elastometry (fibroscan) to predict esophageal varices in patients with viral liver cirrhosis," Ultrasound in Medicine & Biology **41**(6), 1530–1537 (2015).
16. A. Nowicki and K. Dobruch-Sobczak, "Introduction to ultrasound elastography," J Ultrason **16**(65), 113–124 (2016).
17. H. G. Kim, M. S. Park, J. D. Lee, and S. Y. Park, "Ultrasound elastography of the neonatal brain: preliminary study," Journal of Ultrasound in Medicine **36**(7), 1313–1319 (2017).
18. Z. Mei, P. Zheng, X. Tan, Y. Wang, and B. Situ, "Huperzine A alleviates neuroinflammation, oxidative stress and improves cognitive function after repetitive traumatic brain injury," Metabolic Brain Disease **32**(6), 1861–1869 (2017).
19. M. Scholz, V. Noack, I. Pechlivanis, M. Engelhardt, B. Fricke, U. Linstedt, B. Brendel, K. Schmieder, H. Ermert, and A. Harders, "Vibrography during tumor neurosurgery," Journal of ultrasound in medicine **24**(7), 985–992 (2005).
20. A. Martín, E. Macé, R. Boisgard, G. Montaldo, B. Thézé, M. Tanter, and B. Tavitian, "Imaging of perfusion, angiogenesis, and tissue elasticity after stroke," J. Cereb. Blood Flow Metab. **32**(8), 1496–1507 (2012).
21. R. Chandrasekhar, J. Ophir, T. Krouskop, and K. Ophir, "Elastographic image quality vs. tissue motion in vivo," Ultrasound in medicine & biology **32**(6), 847–855 (2006).
22. J. Zhu, X. He, and Z. Chen, "Acoustic radiation force optical coherence elastography for elasticity assessment of soft tissues," Appl. Spectrosc. Rev. **54**(6), 457–481 (2019).
23. Y. Qu, T. Ma, Y. He, J. Zhu, C. Dai, M. Yu, S. Huang, F. Lu, K. K. Shung, and Q. Zhou, "Acoustic radiation force optical coherence elastography of corneal tissue," IEEE J. Sel. Top. Quantum Electron. **22**(3), 288–294 (2016).
24. W. Qi, R. Chen, L. Chou, G. Liu, J. Zhang, Q. Zhou, and Z. Chen, "Phase-resolved acoustic radiation force optical coherence elastography," J. Biomed. Opt. **17**(11), 110505 (2012).

25. Y. Zhu, Y. Zhang, G. Shi, Q. Xue, X. Han, S. Ai, J. Shi, C. Xie, and X. He, "Quantification of iris elasticity using acoustic radiation force optical coherence elastography," Appl. Opt. **59**(34), 10739–10745 (2020).

26. Y. Zhu, Y. Zhao, Y. Zhang, H. Yang, J. Shi, H. Cai, D. Zhang, G. Huang, X. He, and X. Wu, "In vivo evaluation of the effects of SMILE with different amounts of stromal ablation on corneal biomechanics by optical coherence elastography," Diagnostics **13**, 30 (2023).

27. Y. Li, J. Zhu, J. J. Chen, J. Yu, Z. Jin, Y. Miao, A. W. Browne, Q. Zhou, and Z. Chen, "Simultaneously imaging and quantifying in vivo mechanical properties of crystalline lens and cornea using optical coherence elastography with acoustic radiation force excitation," APL photonics **4**(10), 106104 (2019).

28. F. Zvietcovich and K. V. Larin, "Wave-based optical coherence elastography: The 10-year perspective," Prog Biomed Eng (Bristol) **4**, 1 (2022).

29. J. Zhu, Y. Miao, L. Qi, Y. Qu, Y. He, Q. Yang, and Z. Chen, "Longitudinal shear wave imaging for elasticity mapping using optical coherence elastography," Appl. Phys. Lett. **110**(20), 201101 (2017).

30. J. Zhu, J. Yu, Y. Qu, Y. He, Y. Li, Q. Yang, T. Huo, X. He, and Z. Chen, "Coaxial excitation longitudinal shear wave measurement for quantitative elasticity assessment using phase-resolved optical coherence elastography," Opt. Lett. **43**(10), 2388–2391 (2018).

31. F. Zvietcovich, R. G. Gary, H. Mestre, M. Giannetto, M. Nedergaard, J. P. Rolland, and K. J. Parker, "Longitudinal shear waves for elastic characterization of tissues in optical coherence elastography," Biomed. Opt. Express **10**(7), 3699–3718 (2019).

32. P. Boerner, D. Nevozhay, M. Hatamimoslehabadi, H. S. Chawla, F. Zvietcovich, S. Aglyamov, K. V. Larin, and K. V. Sokolov, "Repetitive optical coherence elastography measurements with blinking nanobombs," Biomed. Opt. Express **11**(11), 6659–6673 (2020).

33. C.-H. Liu, D. Nevozhay, A. Schill, M. Singh, S. Das, A. Nair, Z. Han, S. Aglyamov, K. V. Larin, and K. V. Sokolov, "Nanobomb optical coherence elastography," Opt. Lett. **43**(9), 2006–2009 (2018).

34. Y. Zhu, Y. Zhao, J. Shi, T. E. Gomez Alvarez-arenas, H. Yang, H. Cai, D. Zhang, X. He, and X. Wu, "Novel acoustic radiation force optical coherence elastography based on ultrasmall ultrasound transducer for biomechanics evaluation of in vivo cornea," J. Biophotonics **16**(8), e202300074 (2023).

35. J. J. Pitre, M. A. Kirby, D. S. Li, T. T. Shen, R. K. Wang, M. O'Donnell, and I. Pelivanov, "Nearly-incompressible transverse isotropy (NITI) of cornea elasticity: model and experiments with acoustic micro-tapping OCE," Sci. Rep. **10**(1), 12983 (2020).

36. F. Zvietcovich, A. Nair, Y. S. Ambekar, M. Singh, S. R. Aglyamov, M. D. Twa, and K. V. Larin, "Confocal air-coupled ultrasonic optical coherence elastography probe for quantitative biomechanics," Opt. Lett. **45**(23), 6567–6570 (2020).

37. F. Zvietcovich, A. Nair, M. Singh, S. R. Aglyamov, M. D. Twa, and K. V. Larin, "In vivo assessment of corneal biomechanics under a localized cross-linking treatment using confocal air-coupled optical coherence elastography," Biomed. Opt. Express **13**(5), 2644–2654 (2022).

38. Z. Jin, R. Khazaeinezhad, J. Zhu, J. Yu, Y. Qu, Y. He, Y. Li, T. E. Gomez Alvarez-Arenas, F. Lu, and Z. Chen, "In-vivo 3D corneal elasticity using air-coupled ultrasound optical coherence elastography," Biomed. Opt. Express **10**(12), 6272–6285 (2019).

39. Ł. Ambroziński, I. Pelivanov, S. Song, S. J. Yoon, D. Li, L. Gao, T. T. Shen, R. K. Wang, and M. O'Donnell, "Air-coupled acoustic radiation force for non-contact generation of broadband mechanical waves in soft media," Appl. Phys. Lett. **109**(4), 04370 (2016).

40. S. Catheline and N. Benech, "Longitudinal shear wave and transverse dilatational wave in solids," J. Acoust. Soc. Am. **137**(2), EL200–EL205 (2015).

41. X. Han, Y. Zhang, Y. Zhu, G. Shi, Y. Zhao, T. Zhang, C. Xie, J. Shi, G. Huang, and X. He, "A preliminary study of shaker-based optical coherence elastography for assessment of gingival elasticity," Opt. Commun. **503**, 127445 (2022).

42. Y. Jamin, J. K. Boult, J. Li, S. Popov, P. Garteiser, J. L. Ulloa, C. Cummings, G. Box, S. A. Eccles, and C. Jones, "Exploring the biomechanical properties of brain malignancies and their pathologic determinants in vivo with magnetic resonance elastography," Cancer Res. **75**(7), 1216–1224 (2015).

43. X. Jin, F. Zhu, H. Mao, M. Shen, and K. H. Yang, "A comprehensive experimental study on material properties of human brain tissue," Journal of biomechanics **46**(16), 2795–2801 (2013).

44. M. Prange and D. F. Meaney, "Defining brain mechanical properties: effects of region, direction, and species," (SAE Technical Paper, 2000).

45. K. Miller, K. Chinzei, G. Orssengo, and P. Bednarz, "Mechanical properties of brain tissue in-vivo: experiment and computer simulation," Journal of Biomechanics **33**(11), 1369–1376 (2000).